Discrete-Time Direct Model Reference Adaptive Control Application in a High-Precision Inertially Stabilized Platform

Ke Deng, Shuang Cong, *Senior Member, IEEE*, Dejie Kong, and Honghai Shen

***Abstract*—This paper studies the practical use of discrete-time direct adaptive control in a high-precision inertially stabilized platform's turbulence isolation system for the purpose of enhancing isolation performance. Under low-frequency and low-velocity environments, the velocity-stabilized loop of the platform shows severe nonlinear characteristic; therefore, its isolation performance is limited. In previous research, we constructed a nonlinear model of the velocity-stabilized loop by using an improved Stribeck friction model, and also designed a feed-forward compensation strategy. Both have obtained outstanding performance during practical experiments. However, errors still exist as disturbance of the unmodeled part and environmental change causes the system's parameter to vary. To solve this, a novel discrete-time direct model reference adaptive control based on nonlinear friction compensation is introduced to the original proportional-integral control system. An improved projection algorithm and a recursive least-square algorithm with fading memory are respectively used to design the adaptive law. By using a turbulence observer to provide a reference signal, both types of controls are applied to the carrier turbulence isolation system. Results of the practical experiments prove that model reference adaptive control can further enhance the system's isolation ability.**

***Index Terms*—Adaptive control, inertially stabilized platform (ISP), model reference adaptive control, nonlinear friction, turbulence isolation.**

Manuscript received September 24, 2017; revised January 25, 2018 and March 7, 2018; accepted April 6, 2018. Date of publication April 27, 2018; date of current version August 31, 2018. This work was supported in part by the Projects of Ultra-Precision Control System Joint Laboratory of USTC under Grant KD1012210167 and in part by the National Natural Science Foundation of China under Grant 61573330. *(Corresponding author: Shuang Cong.)*

K. Deng is with the State Key Laboratory of Air Traffic Management System and Technology, Nanjing 210001, China (e-mail: dengke@mail.ustc.edu.cn). (e-mail: dengke@mail.ustc.edu.cn).

S. Cong is with the , Department of AutomationUniversity of Science and Technology of China, Hefei 230027, China (e-mail: scong@ustc.edu.cn). (e-mail: scong@ustc.edu.cn).

D. Kong is with the , Department of Optoelectronic EngineeringChangchun University of Science and Technology, Changchun 130022, China (e-mail: kongdejie78@126.com). (e-mail: kongdejie78@126.com).

H. Shen is with the , Key Laboratory of Aviation Optical Imaging and MeasurementChangchun Institute of Optics, Fine Mechanics and Physics,, Chinese Academy of Sciences, Changchun 130022, China (e-mail: shenhh@ciomp.ac.cn). (e-mail: shenhh@ciomp.ac.cn).

Digital Object Identifier 10.1109/TIE.2018.2831181

I. Introduction

INERTIALLY stabilized platform (ISP) is the core device used in navigation, guidance, and measurement applications. It is used to isolate carrier turbulence and stabilize the optical equipment, so the equipment can keep its orientation or maintain line-of-sight [1]. It has a wide range of use in both civil and military applications [2], [3] such as aircraft, ships, and electron telescopes. Furthermore, high-precision ISP is one of the most important components in the present day sophisticated military equipment. The stabilization accuracy of the optical axis is one of the key performance indexes of ISP, and it directly impacts its tolerance toward carrier turbulence. This is currently reduced to microradian magnitude (μrad). ISP is a complicated control system, and it is affected by various disturbances, for example, nonlinear frictions, gyrodrift, and mechanical resonance. Under the assumption that the hardware of ISP is fixed, the key to further improve accuracy lies within analyzing errors and how they affect the system, and then designing a strategy to compensate them. Accurate modeling of the platform is the most effective method to analyze the errors.

ISP requires high stabilization precision and quick real-time feedback [4], especially because the optical equipment it carries already faces the problem of time lapse during identification and analysis of the target. Due to its high practical usage, a linear controller with a simple design and structure, such as proportional-integral-differential (PID) compensator, is widely used on ISP. However, its ability to further increase stabilization precision faces two limitations. First, under low-frequency and low-velocity environment, nonlinear friction causes the quality of the control system to significantly decrease [5]. Second, when environment change occurs, it is unable to overcome the control error that is brought by parameter variations of the system.

For the first limitation, nonlinear modeling and friction compensation are effective methods to rectify it. Currently, friction compensation is a necessary process in high-precision control system [6], and it has been split into model-based and model-free. The key to model-based friction compensation is to select the proper friction model and to identify important parameters [7]. Various types of friction models [8] are currently being studied, and are split into static friction model and dynamic friction model. The static friction models, i.e., Stribeck model [8], have a simple and practical structure, but they face problems such

as a lack of precision and switching of model equations. While dynamic models, i.e., Lugre model [9], are more precise, their structure and parameter tuning are more complicated. Model-free friction compensation, which is based on disturbance observer [10], combines friction and other disturbance into overall disturbance [11]. Through the aid of an observer to inhibit the overall disturbance, the effect of friction is then removed.

For the second limitation, adaptive control can be introduced to reduce the impact of time-varying parameters. Model reference adaptive control (MRAC) is an important type of adaptive control; it has been widely used and studied both theoretically and practically. MRAC has developed from being applied to continuous-time systems to now discrete-time systems. From the aspect of design, it has already developed from an optimal local parameter method, i.e., MIT method, to two main types of stability theorem: Lyapunov stability theorem and Popov hyperstability theorem. MRAC is equivalent to the nonlinear time-varying feedback system, and Lyapunov function is a powerful tool in solving its stability. The second theorem of Lyapunov is more frequently used to design MRAC, and this method is further divided into direct and indirect types. In direct MRAC, it directly amends the parameter in the controller, while in indirect MRAC, it estimates the parameters of the model of controlled process, and then amends the controller's parameter through obtaining the correlation between the controller's and the model's parameters. Studies have shown that the order of adaptive law in indirect MRAC's is lower than direct MRAC; however, analyzing its stability is more difficult [12]. In recent years, MRAC has been widely studied and developed, especially on robustness. L1 adaptive control (L1-AC) [13] adopts a strictly stable filter to filter the input signals, which is used to obtain faster convergence. However, recent researches have shown that when compared to standard MRAC, the stability margin of robustness has actually been reduced [14]. By incorporating a proportional-integral (PI) compensator in the feedback loop of MRAC architecture [15], the controller achieves guaranteed transient and steady-state performance with improved robustness. An improved discrete-time MRAC is designed to cope with automotive device's nonlinear and discontinuous dynamics [16], and it extends the class of the minimal control synthesis algorithms for discrete-time systems. Adding a saturation function and a PI controller, a modified version of variable structure MRAC (VS-MRAC) schema is developed, and it is applied to the fault-tolerant control [17]. A predictive model reference adaptive system (MRAS) speed estimator based on the finite control set-model predictive control (FCS-MPC) principle is proposed for sensorless induction motor [18]. With an external filter, the MRAC method is proposed to not only stabilize the error system but also guarantee its transient performance for a class of nonlinear systems with uncertain parameters, disturbance, and unmodeled dynamics [19]. In addition, neural networks have been introduced into adaptive control architecture to improve both transient and steady-state performance [20]–[22]. As shown, there are a lot of different design methods for MRAC; however, how to fuse them into practical application is a hurdle. This hurdle is especially difficult in a high-precision control system.

In this paper, we will develop a novel discrete-time direct MRAC method to overcome the turbulence isolation problem of ISP's velocity-stabilized loop. By adopting an upgraded strategy, this MRAC method is designed to overcome errors due to disturbance of the unmodeled part and environmental change based on the original PI control system, in addition to the previous work on nonlinear friction compensation. Unlike other MRAC methods, it constructs a schema through model matching, in which a class of parameter-optimization algorithms can be used to obtain adaptive laws. Improved projection algorithm and recursive least-square algorithm with fading memory are respectively used to design the law. After stability analysis and simulations, practical experiments have been conducted with the aid of the refine-designed turbulence observer, which is used to provide a reference signal. All this would assist the system to achieve a better isolation performance, which is the main contribution of this paper. In addition, this is the first time the discrete-time direct MRAC method has been applied to high-precision ISP with microradian magnitude.

This paper is organized as follows. In Section II, we review the previous work on nonlinear modeling and friction compensation. In Section III MRAC is designed, and then we conduct stabilization analysis and simulation. In Section IV, we perform practical experiments on ISP using MRAC. Finally, a conclusion is drawn in Section V.

II. Nonlinear Modeling and Feed-Forward Compensation

Here, we describe our previous work on nonlinear friction modeling and feed-forward compensation based on original PI control system; these provide the foundation of our MRAC.

In our previous research, we have concluded that the nonlinear friction is the main factor that influences isolation performance in low-frequency and low-velocity environment. To resolve it, a nonlinear model of velocity-stabilized loop was constructed and the corresponding friction compensation strategy was designed and verified. The specific about this research is published in [23].

Two axes four-gimbal ISP consists of inner/outer azimuth gimbal and inner/outer elevation gimbal. Within the inner gimbal lies the velocity-stabilized loop, which is the key component toward isolating turbulence. It uses rate gyros as the feedback sensors, and its performance has a direct effect on the stabilization precision of ISP. The performance indicator is based on its capability to isolate carrier turbulence. Assume isolation ϕ is

$$\phi = |\boldsymbol{\omega} + \boldsymbol{\omega}_2|_{\max} / |\boldsymbol{\omega}|_{\max} = |\boldsymbol{\omega}_1|_{\max} / |\boldsymbol{\omega}|_{\max} \tag{1}$$

where $\boldsymbol{\omega}_1$ is the angular velocity vector of the platform related to the inertia space, $\boldsymbol{\omega}_2$ is the angular velocity vector of the platform relative to the carrier, and $\boldsymbol{\omega}$ is the turbulence angular velocity vector of the carrier relative to inertia space, where $\boldsymbol{\omega}_1 = \boldsymbol{\omega} + \boldsymbol{\omega}_2$. Assume that the reference signal is zero, which means maintaining an orientation. Hence, the lower the value of ϕ, the better the ISP is able to isolate turbulence. It is noteworthy that these max values in (1) should be measured when the ISP

is in stable operation and the sampling time span is at least one period of turbulence signal.

A. Nonlinear Modeling

To have an insight into friction, we have conducted the nonlinear modeling of velocity-stabilized loop.

The velocity-stabilized loop of the inner azimuth gimbal is used as an example. By using the balance equations of the driving torque of the dc torque motor and the armature voltage, and by considering the effect of the current loop and neglecting the armature inductance, the model of the velocity-stabilized loop is obtained and simplified. It can be divided into a first-order linear system part and a nonlinear friction part $T_f(k)$.

According to the classic Stribeck model [8], friction torque only correlates to angular velocity. However, actual friction torque is also affected by the gimbal's position. Distinguishing different movement directions and different half-planes, the complete movement of the inner azimuth gimbal consists of four submovements. Based on above, an improved Stribeck nonlinear friction model with high precision is proposed.

Combining the nonlinear friction model with the linear model, we have obtained the nonlinear model of the velocity-stabilized loop, which has 24 parameters that need to be identified. Based on the designed identification signal, we thereby utilize the genetic algorithm (GA) within the optimization toolbox in MATLAB. The fitness function of GA minimizes the root-mean-square error (RMSE) between the model output and measured output. We obtain the results at 95% confidence level. With average RMSE of 0.134 °/s, it is only 3.8% of the absolute maximum amplitude of the input signal. Last, model verifications are conducted by another four sets of data and some simulation tests. The details of the parameters of model, the configurations of GA, and the process of verification are in [23].

B. Friction Feed-Forward Compensation

To overcome the negative effect of nonlinear friction, we have conducted the friction feed-forward compensation.

Based on the nonlinear model above, the friction feed-forward compensation can be conducted by extracting the nonlinear friction part. However, adjustment needs to be made when designing the model-based compensation strategy. First, to facilitate the addition to the control quantity, the compensation quantity of friction is converted to control voltage $T_f(k)/K_e$, where K_e is the equivalent model of the amplifier. Second, because the nonlinear friction model has several equations, the compensation quantity would change between them during the actual usage, causing the system to tremble. To prevent the tremble causing mechanical resonance, the compensation quantity is smoothly filtered. Last, due to the unmodeled part and other nonlinear disturbances, differences exist between friction model and real friction. Under compensated friction would lead to steady-state error, while over compensation would lead to limited cycle oscillation [24]. To prevent oscillation causing the system to be unstable, an attenuation factor γ is introduced to make sure that the entire system is maintained at slightly under-compensation state.

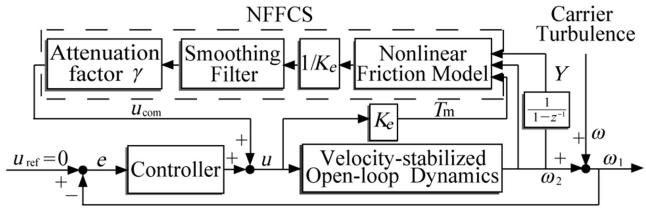

Fig. 1. Carrier turbulence isolation system with nonlinear friction feed-forward compensation.

Combining the nonlinear friction feed-forward compensation strategy (NFFCS) into the actual carrier turbulence isolation system, we have produced control system (see Fig. 1). The turntable stimulates the angular velocity ω during carrier turbulence. ISP uses reference signal $u_{\text{ref}} = 0$ to achieve line-of-sight stabilization.

During practical experiments, the azimuth control system requires the inner and outer azimuth gimbals to work in coordination. The movement of the outer azimuth gimbal follows the inner gimbal and provides expansion of rotation range and wind resistance isolation. The controller of the inner gimbal consists of PI controller, notch filter, and bound of control quantity. Ten groups of experiments with the same turbulence (position signal of 3°, 1/6 Hz) were separately conducted on the original PI control system and control system with the nonlinear friction compensation (PI+NFFCS). Results prove that when compared to the PI, the PI+NFFCS has shown enhanced performance. Average isolation has decreased from 23.01% to 13.40%, so the isolation performance has increased by 41.76%. It shows that the compensation strategy significantly inhibits nonlinear friction, and increases the control system's isolation ability against carrier turbulence. The details of the parameters of the controller, the configurations of NFFCS, and the results analysis of experiments are in [23].

III. Design of Discrete-Time Direct MRAC

By using NFFCS the isolation performance has been significantly improved, but there is still room for further improvements. As a low-pass filter has been used, the main factor that now affects the performance is parameter change caused by the unmodeled part and environmental change. Additionally, according to the isolation system in Fig. 1, it is equivalent to the velocity ω_2 to track the reverse value of the carrier turbulence ω, $\omega_2 \to -\omega$ when $u_{\text{ref}} = 0$. Hence, we can design discrete-time direct MRAC to further increase its isolation performance and ensure that it has stability.

A. Model Matching

Transforming the turbulence isolating problem to the turbulence tracking problem, during the design of the MRAC, we can then set the reverse value of the carrier turbulence $-\omega$ as the reference signal. After friction compensation, the nonlinearity of the original closed-loop control system has nearly been suppressed. We assume that the closed-loop system approximates to a linear model $B(z)/A(z)$. The reference model is set

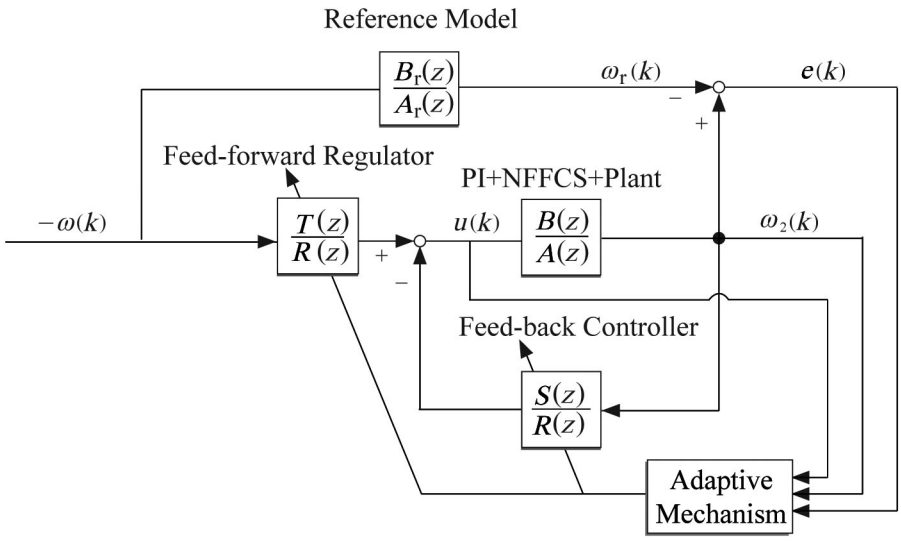

Fig. 2. Discrete-time direct MRAC in turbulence tracking system.

as $B_r(z)/A_r(z)$. Select feed-forward regulator plus feed-back controller as model matching, and set them as $T(z)/R(z)$ and $S(z)/R(z)$,respectively. We then obtained the MRAC structure (see Fig. 2).

Set the degrees of $A(z)$, $B(z)$, $A_r(z)$, $B_r(z)$, $S(z)$, $R(z)$, and $T(z)$ as n, m, n_r, m_r, n_S, n_R, and n_T, respectively. As for the controlled process, assume $n > m$, $A(z)$, and $B(z)$ are coprime, $B(z)$ is stable, and its highest order coefficient b_0 is known. As for the reference model, assume $A_r(z)$ is monic and stable and the time-delay of the reference model and controlled process is the same, which means $d = n - m = n_r - m_r$.

In the tracking system in Fig. 2, we hope the system output $\omega_2(k)$ can be equal to the reference input $-\omega(k)$ at all the time; therefore, set reference model as $1/z^{n_k}$, where n_k is the computer time-delay and is set as one. According to the fitted curves under some linear models' parameter identifications, the PI+NFFCS+Plant closed-loop control system shows high linearity. Based on several experimental tests, we assume that a first-order linear model can approximate it. Then, we have

$$\begin{cases} B(z)/A(z) = b_0/(z + a_1) \\ B_r(z)/A_r(z) = 1/z \end{cases}. \tag{2}$$

If the output $\omega_2(k)$ is equal to reference model output $\omega_r(k)$, then the transfer function should satisfy

$$B(z)T(z)/(A(z)R(z) + B(z)S(z)) = B_r(z)/A_r(z) \tag{3}$$

where if $A(z)$, $B(z)$, $A_r(z)$, and $B_r(z)$ are known, then the problem turns into solving $S(z)$, $R(z)$, and $T(z)$.

To make the derivation easier, set $T(z) = B_r(z) = 1$, then $S(z)$ and $R(z)$ still need to satisfy

$$A(z)R(z) + B(z)S(z) = A_r(z)B(z). \tag{4}$$

Set $S(z)$ and $R(z)$ as

$$\begin{cases} S(z) = s_0 z^{n_S} + s_1 z^{n_S - 1} + \cdots + s_{n_S} \\ R(z) = r_0 z^{n_R} + r_1 z^{n_R - 1} + \cdots + r_{n_R} \end{cases}. \tag{5}$$

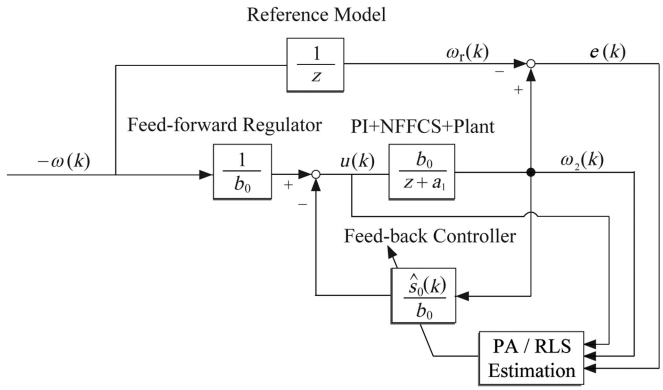

Fig. 3. Discrete-time direct MRAC based on the PA/RLS in turbulence tracking system.

Substituting (2) and (5) into (4), we can obtain $S(z) = s_0 = -a_1$ and $R(z) = r_0 = b_0$. Therefore, the feed-forward regulator and feed-back controller are

$$\begin{cases} T(z)/R(z) = 1/r_0 = 1/b_0 \\ S(z)/R(z) = s_0/r_0 = -a_1/b_0 \end{cases}. \tag{6}$$

From Fig. 2 and (6), we can obtain the control law as

$$u(k) = -(1/r_0)\left[s_0(k)\omega_2(k) - (-\omega(k))\right] \tag{7}$$

where $r_0 = b_0$, and have previously assumed that b_0 is known. Therefore, when system parameters are changed, we can adjust the parameter s_0 to update the control law. Then, by using (6) to adjust the controller, we achieve direct adaptive control. Projection algorithm (PA) and recursive least-square (RLS) algorithm have been used to optimally estimate the parameter s_0. The detailed control structure is shown in Fig. 3, where $\hat{s}_0(k)$ is the estimated value of s_0.

B. Adaptive Law Based on the Improved PA

PA is a type of stochastic gradient algorithm, and it is used to solve the minimum value problem when there are constraints. According to Fig. 3, we set the cost function as

$$J_{\mathrm{PA}}(\hat{s}_0(k),\hat{s}_0(k-1),k)=\frac{1}{2}|\hat{s}_0(k)-\hat{s}_0(k-1)|^2 + \lambda\left[\omega_2(k)-b_0u(k-d)-\omega_2(k-d)\hat{s}_0(k)\right] \quad (8)$$

where λ is the Lagrange multiplier and d is the time delay, which is $d=n-m=1$. The cost function is split into two halves: the first half is used to obtain the minimum error of the parameter, while the latter half is constrained.

According to the cost function, we can deduce the $\hat{s}_0(k)$ recurrence equation as

$$\hat{s}_0(k)=\hat{s}_0(k-1)+(1/(\omega_2(k-1))) \times\left[\omega_2(k)-b_0u(k-1)-\omega_2(k-1)\hat{s}_0(k-1)\right]. \quad (9)$$

There are some shortcomings when (9) is used in ISP. Its incremental factor $1/\omega_2(k-1)$ will lead to the control law to cause strong tremble when velocity changes directions. To improve the algorithm, we add the iterative formula $\rho(k)$

$$\rho(k)=\lambda_{\mathrm{PA}}\rho(k-1)+\omega_2(k-1)^2 \quad (10)$$

where λ_{PA} is the forgetting factor, and $\lambda_{\mathrm{PA}}\in[0.9,0.999]$. Set the initial $\rho(0)=1$. Amend the incremental factor in (11) into $\omega_2(k-1)/\rho(k)$, we obtained the following formula:

$$\hat{s}_0(k)=\hat{s}_0(k-1)+(\omega_2(k-1)/\rho(k)) \times\left[\omega_2(k)-b_0u(k-1)-\omega_2(k-1)\hat{s}_0(k-1)\right] \quad (11)$$

where $\rho(k)$ under the condition that $\rho(0)=1$ ensures that the increment will not abruptly change. At the same time, the forgetting factor λ_{PA} gives the algorithm the ability to track the time-varying parameter.

C. Adaptive Law Based on the Fading Memory RLS

The RLS algorithm minimizes sum of squared errors and is widely used in engineering. Applying it to Fig. 3, we set the cost function with exponential window

$$J_{\mathrm{RLS}}(\hat{s}_0(k),k)=\sum_{i=d}^{k}\lambda_{\mathrm{RLS}}^{k-i}\left(\omega_2(i)-b_0u(i-d) -\omega_2(i-d)\hat{s}_0(k)\right)^2 \quad (12)$$

where $k\geq d$ and $d=n-m=1$. λ_{RLS} is the forgetting factor, and $\lambda_{\mathrm{RLS}}\in[0.9,0.999]$.

The introduction of the forgetting factor eliminates the data saturation problem and allows the algorithm to have the ability to track the time-varying parameter. According to (12), we can derive the recursive equation of $\hat{s}_0(k)$

$$\begin{cases}\hat{s}_0(k)=\hat{s}_0(k-1)+\frac{P(k-1)\omega_2(k-1)}{\lambda_{\mathrm{RLS}}+P(k-1)\omega_2(k-1)^2} \times\left[\omega_2(k)-b_0u(k-1)-\omega_2(k-1)\hat{s}_0(k-1)\right] \\ P(k)=\frac{1}{\lambda_{\mathrm{RLS}}}\left(P(k-1)-\frac{P(k-1)^2\omega_2(k-1)^2}{\lambda_{\mathrm{RLS}}+P(k-1)\omega_2(k-1)^2}\right)\end{cases} \quad (13)$$

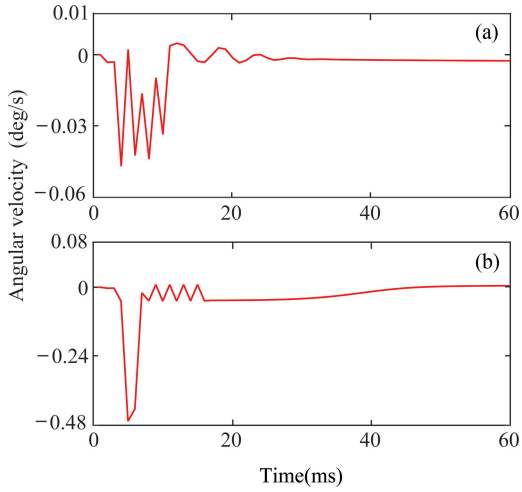

Fig. 4. Tracking error $\omega_2(k)-(-\omega(k))$ curve during the beginning 60 ms in simulation. (a) MRAC based on improved PA. (b) MRAC based on fading memory RLS.

where selecting a large positive value of $P(0)$ can eliminate the influence caused by initial value. The smaller the λ_{RLS}, the stronger the ability to track changes in the parameter; however, if it is too small, the parameter will present large fluctuation.

D. Stability Analysis and Simulations

The system shown in Fig. 3 is a compound control system. It consists of the original PI closed-loop control system, the NFFCS, and the MRAC. Its stability is the primary concern, but we also expect the illustration to be simple.

The MRAC's controlled process is the PI+NFFCS+Plant. After debugging parameters, the original PI closed-loop control system can be stable during runtime. Adding NFFCS with a slight adjustment will not affect its stability, as the feed-forward compensation does not change the solutions of the characteristic equation. Hence, the controlled process is stable.

The method behind how to prove the stability of MRAC is to build error dynamic equations for model matching and parameter estimation. Then, designing a Lyapunov function that combines the two errors and proving that the difference equation is below zero. The proof process is complex; however, it is supported by the related theory [25]. We will only provide the conclusion here: In both types of discrete-time direct MRAC, when the reference input $-\omega(k)$ is bounded, the control system is Lyapunov stable.

To test the performance of the both types of MRAC under nonlinear disturbance, we have designed an exaggerated simulation experiment in which the quantity of friction compensation is reduced by half. The simulation system is set up based on Fig. 3, and the parameters used are given in Sections II.B, III.B, and III.C. During simulation, input $-\omega(k)$ is given by velocity with π°/s , 1/6 Hz. To obtain the optimal performance under each MRAC, we have used trial and error and found the proper parameters as $\lambda_{\mathrm{PA}}=0.99$ and $\lambda_{\mathrm{RLS}}=0.95$. Fig. 4 shows the tracking error curve $\omega_2(k)-(-\omega(k))$ during the first 60 ms. We can observe the adaptive processes of the two MRACs. The

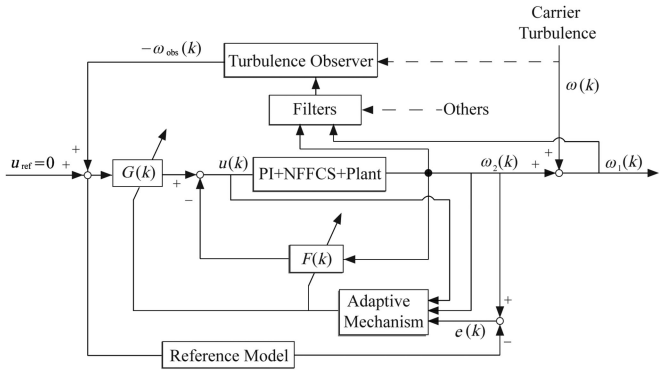

Fig. 5. Carrier's turbulence isolation system with discrete time direct MRAC.

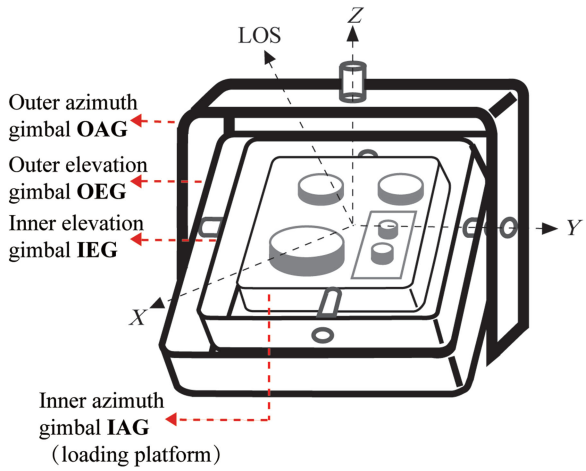

Fig. 6. 3-D structure graphs of the ISP used in experiments.

convergence rate of the MRAC based on fading memory RLS is faster than that based on enhanced PA, but the initial error is larger.

Furthermore, we have observed the curve under stable state and found that fluctuation occurs when the velocity of the gimbal is close to zero. Through calculation of one period with 6000 ms, the isolation of the MRAC based on PA is 1.36%, and that of the MRAC based on RLS is 1.53%. The results prove the feasibility of the both MRAC.

IV. Experiments

Even after applying the MRAC designed to the ISP, we would still need to solve three key problems. First, we need to covert the turbulence tracking system in Fig. 3 into the original isolation system. Second, the carrier turbulence, which is provided by turntable with predefined amplitude and frequency, has no sensor to provide the real-time value of the turbulence for MRAC's reference signal. Hence, we need to design a real-time turbulence observer to overcome it. Last, to facilitate the setup of the initial parameters of the MRAC, we need to perform identification on the general controlled process, which is PI+NFFCS+Plant. Based on all above-mentioned problems, we then conduct experiments to examine the MRAC.

A. Convert to Turbulence Isolation System With MRAC

When implementing the MRAC from turbulence tracking system to isolation system in practical work, we need to adjust the inner and outer azimuth gimbals' joint control system. For the convenience of this section, we will temporary ignore the outer gimbal control system's part, and single out the inner gimbal's MRAC system, as shown in Fig. 5.

As shown in the figure, the input signal $u_{\rm ref}=0$. The reference signal of MRAC is $-\omega_{\rm obs}(k)$, which is the reverse of the turbulence's observation value. PI+NFFCS+Plant is the general controlled process. According to Fig. 3, the feed-forward regulator is $G(k)=1/b_0$, and it is fixed. The feed-back controller is $F(k)=\hat{s}_0(k)/b_0$, and it is adjustable. The reference model is $1/z$. The adaptive mechanism varies according to the estimation method of PA or RLS. The output $\omega_1(k)$ is the velocity of the gimbal relative to the inertial space. Within the isolation system, the carriers' turbulence $\omega(k)$ is provided by the turntable from the outside. Therefore, we should construct a turbulence observer.

B. Design of the Carrier's Turbulence Observer

According to the ISP's active isolation principle and (1), when only considering the azimuth turbulence, it is known that $\omega=\omega_1-\omega_2$. Note that ω_2 is the inner azimuth gimbal's rotation rate relative to the carrier. In reality, we can only obtain $\hat{\omega}_2$ by the resolver, which is the inner azimuth gimbal's rotation rate relative to the outer gimbal. Obviously, most of the time, $\hat{\omega}_2\neq\omega_2$. To obtain the real-time turbulence signal for MRAC, we approach this by looking at the coupled kinematic equations.

The ISP's three-dimensional (3-D) structure graphs are presented in Fig. 6. From inside out, it consists of the inner azimuth gimbal IAG (loading optical devices), the inner elevation gimbal IEG, the outer elevation gimbal OEG, and the outer azimuth gimbal OAG.

According to this, we place the ISP's motion decomposition on the five coordinates within the 3-D space. From outward inward, they are carrier coordinate $OX_BY_BZ_B$, OAG's coordinate $OX_AY_AZ_A$, OEG's coordinate $OX_EY_EZ_E$, IEG's coordinate $OX_eY_eZ_e$, and IAG's coordinate $OX_aY_aZ_a$. Within a small period Δt, assume that the OAG rotates θ_A around axis OZ_B, the OEG rotates θ_E around axis OY_A, the IEG rotates θ_e around axis OY_E and the IAG rotates θ_a around axis OZ_e. The relationships between them are $OZ_B=OZ_A$, $OZ_e=OZ_a$, and $OY_A=OY_E=OY_e$. Hence, we obtained Fig. 7.

Assume the velocity vectors relative to initial space of the carrier's turbulence, OAG, OEG, IEG, and IAG, are ω_B, ω_A, ω_E, ω_e, and ω_a, respectively. $T_{\rm BA}$, $T_{\rm AE}$, $T_{\rm Ee}$, and $T_{\rm ea}$ are defined as transformation matrixes of the five coordinates from outside to inside. Hence, we obtained the following kinetic equations:

$$\begin{cases}\omega_A=T_{\rm BA}\omega_B+[0\ \ 0\ \ \dot{\theta}_{\rm A}\ ]^T,\omega_E=T_{\rm AE}\omega_{\rm A}+[0\ \ \dot{\theta}_E\ \ 0]^T\\ \omega_e=T_{\rm Ee}\omega_E+[0\ \ \dot{\theta}_{\rm e}\ \ 0]^T,\omega_a=T_{\rm ea}\omega_e+[0\ \ 0\ \ \dot{\theta}_a\ ]^T\end{cases}\tag{14}$$

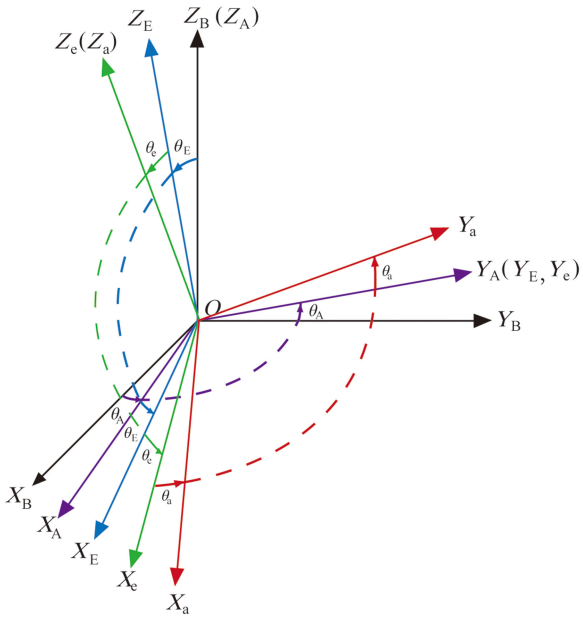

Fig. 7. Decomposition of coupled motion of the multi-gimbal ISP.

where the matrixes $T_{\rm BA}$, $T_{\rm AE}$, $T_{\rm Ee}$, and T_{ea} are

$$T_{\rm BA}=\begin{bmatrix}\cos\theta_A & \sin\theta_A & 0\\ -\sin\theta_A & \cos\theta_A & 0\\ 0 & 0 & 1\end{bmatrix},$$

$$T_{\rm AE}=\begin{bmatrix}\cos\theta_E & 0 & -\sin\theta_E\\ 0 & 1 & 0\\ \sin\theta_E & 0 & \cos\theta_E\end{bmatrix}$$

$$T_{\rm Ee}=\begin{bmatrix}\cos\theta_e & 0 & -\sin\theta_e\\ 0 & 1 & 0\\ \sin\theta_e & 0 & \cos\theta_e\end{bmatrix},T_{\rm ea}=\begin{bmatrix}\cos\theta_a & \sin\theta_a & 0\\ -\sin\theta_a & \cos\theta_a & 0\\ 0 & 0 & 1\end{bmatrix}. \tag{15}$$

Combining (14) and (15), the velocity vector ω_a is

$$\begin{aligned}\omega_a=&\,T_{\rm ea}T_{\rm Ee}T_{\rm AE}T_{\rm BA}\omega_B+T_{\rm ea}T_{\rm Ee}T_{\rm AE}\begin{bmatrix}0 & 0 & \dot\theta_A\end{bmatrix}^T\\&+T_{\rm ea}T_{\rm Ee}\begin{bmatrix}0 & \dot\theta_E & 0\end{bmatrix}^T+T_{\rm ea}\begin{bmatrix}0 & \dot\theta_e & 0\end{bmatrix}^T\\&+\begin{bmatrix}0 & 0 & \dot\theta_a\end{bmatrix}^T.\end{aligned} \tag{16}$$

When only considering the azimuth motion relative to inertial space, the corresponding component of vector ω_a is needed. According to Fig. 5, ω_a becomes ω_1, $\dot\theta_a$ is the rotatory velocity $\hat\omega_2(k)$, the turbulence's azimuth component is $\omega_{Bz}=\omega$. Therefore, ω_1 is

$$\begin{aligned}\omega_1=&\,(\omega_{Bx}\cos\theta_A+\omega_{By}\sin\theta_A)\\&\times(\sin\theta_e\cos\theta_E+\cos\theta_e\sin\theta_E)\\&+(\omega+\dot\theta_A)(\cos\theta_e\cos\theta_E-\sin\theta_e\sin\theta_E)+\hat\omega_2.\end{aligned} \tag{17}$$

During experiments, the 3-D turntable is set to only provide azimuth turbulence; hence, $\omega_{Bx}=\omega_{By}=0$. Simplifying (17), we can obtain the azimuth turbulence ω. Hence, the turbulence observer is designed as the following equation:

$$\omega_{\rm obs}=\omega=(\omega_1-\hat\omega_2)/(\cos\theta_e\cos\theta_E-\sin\theta_e\sin\theta_E)-\hat\omega_{2A} \tag{18}$$

where ω_1 and $\hat\omega_2$ are provided by the flexible rate gyro and the resolver fixed on the IAG, respectively. $\hat\omega_{2A}=\dot\theta_A$ is provided by resolver fixed on the OAG. θ_e and θ_E are provided by resolvers fixed on the IEG and OEG, respectively. Additionally, some filters are designed for these measured values. During experiments, we compared $\omega_{\rm obs}$ with the set turbulence signal. The observer is verified, but we will not get into details here.

C. Identification of the General Controlled Process

To obtain b_0 and initial $\hat s_0(k)$ for the MRAC, the model of general controlled process needs to be identified.

From Section II and [23], we know that PI+NFFCS+Plant shows a high linearity. To approach the general controlled process of MRAC, we use the following first-order linear model:

$$\omega_2(k)=\hat a\omega_2(k-1)+\hat bu(k-1) \tag{19}$$

where $\hat a$ and $\hat b$ are parameters to be identified.

Since the frequency of carrier turbulence in experiments is 1/6 Hz, the identification signal is designed as

$$\begin{aligned}u(k)=&\,(1/2)\pi\cos(2\pi\cdot1/6k)+(1/3)\pi\cos(2\pi\cdot1/3k)\\&+(1/6)\pi\cos(2\pi\cdot1/2k)\end{aligned} \tag{20}$$

where the unit of the input signal is °/s.

For higher accuracy identification, we then differentiate the parameters $\hat a$ and $\hat b$ in (19) during ISP gimbal's positive and negative movements. Take the inner azimuth gimbal for example, set the *X*-axis as the optical axis of optic-electronic equipment when the gimbal is at the center 0° position; set the *Y*-axis as the range of the rotation angle, and it is between ±4 °. The *X*-axis is perpendicular to the *Y*-axis. Thus, $Y\le0$ indicates that the position is on the left half plane, and $Y>0$ indicates that the position is on the right half plane. Suppose the speed ω_2 is the positive direction of movement when the gimbal moves from the left half plane to the right half plane, that is, the negative direction is under the opposite condition. Hence, the complete movement of the inner azimuth gimbal is consisted of two submovements. We use "+" and "−" to label the respective positive and negative directions of the gimbal's motions, respectively.

In practice, we place the ISP on a horizontal desktop. Then, the identification signal (20) is input into the PI+NFFCS control system of the inner azimuth gimbal. The I/O data of the system is obtained for parameter identification use.

Using the method in Section II, the GA toolbox of MATLAB is also employed for parameter identification, and the results are shown in Table I. The RMSE of the model is 0.1532 °/s, which only takes up 4.88% of the input signal's absolute amplitude π °/s. The results provide useful information for the initial tuning of the MRAC. According to (5) and (6), we can set $b_0=(\hat b^+\hat b^-)^{1/2}=0.9827$, and initial value of $\hat s_0(k)$ as $\hat s_0(0)=(\hat a^+\hat a^-)^{1/2}=7.07{\rm E}-7$. This will help the MRAC method to fast implement line-of-sight stabilization, avoiding large initial oscillation.

TABLE I
RESULTS OF THE PARAMETERS IDENTIFICATION FOR GENERAL CONTROLLED PROCESS

Parameters	Values
$\hat{a}^+$	1.3672×10^(-6)
$\hat{b}^+$	0.9921
$\hat{a}^-$	3.6532×10^(-7)
$\hat{b}^-$	0.9734
RMSE	0.1532 deg/s

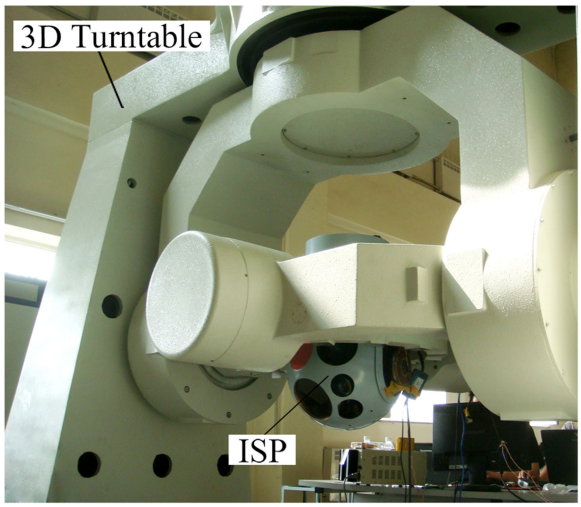

Fig. 8. Two axes four-gimbal ISP and 3-D flight simulation turntable in actual experiments.

TABLE II
ISOLATIONS OF THE TURBULENCE ISOLATION SYSTEM WITH PA-MRAC

Controller	Isolation ϕ (%)					Average
PA-MRAC	8.96	9.35	8.63	9.84	8.62	9.11%
	9.04	8.80	8.10	9.97	9.80	

D. Experiments of the Discrete-Time Direct MRAC Based on Improved PA

According to Fig. 5, (6), and (7), we obtain the control law as

$$u(k) = -(1/b_0)\left[\hat{s}_0(k)\omega_2(k) - (u_{\text{ref}} - \omega_{\text{obs}}(k))\right] \qquad (21)$$

where the iterative equations for $\hat{s}_0(k)$ are (10) and (11). Referring to the simulation results, we set $\lambda_{\text{PA}} = 0.99$ and $\rho(0) = 1$. Set $b_0 = 0.9827$ and $\hat{s}_0(0) = 7.07 \times 10^{-7}$.

In experiments, the ISP is fixed on the 3-D flight simulation turntable, as shown in Fig. 8. The input azimuth turbulence is provided by the turntable with sinusoidal position signal, which can then be converted to the velocity $\omega(k)$ with π °/s and 1/6 Hz. The output is $\omega_1(k)$ with unit °/s.

Ten groups of experiments are done to the combined control system (labeled as PA-MRAC) and the results are given in Table II. The average isolation is 9.11%. In one experiment, the isolation performance and the corresponding $\hat{s}_0(k)$ are shown in Fig. 9. Through calculation, the isolation is 8.10%.

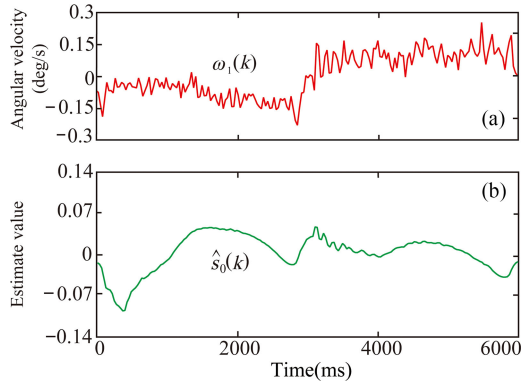

Fig. 9. Results of the turbulence isolation system with PA-MRAC. (a) $\omega_1(k)$ curve. (b) $\hat{s}_0(k)$ curve.

TABLE III
ISOLATIONS OF THE TURBULENCE ISOLATION SYSTEM WITH RLS-MRAC

Controller	Isolation ϕ (%)					Average
RLS-MRAC	9.81	9.11	10.06	9.12	9.52	9.68%
	9.57	10.48	10.72	8.56	9.86	

E. Experiments of the Discrete-Time Direct MRAC Based on Fading Memory RLS

The system's control law is also given as (21) and the recursive estimation equation of $\hat{s}_0(k)$ is given by (13). Set $\lambda_{\text{RLS}} = 0.95$, $P(0) = 1000$, $b_0 = 0.9827$, and $\hat{s}_0(0) = 7.07 \times 10^{-7}$. Ten groups of experiments on such control system (labeled as RLS-MRAC) are conducted and the results are shown in Table III. The average isolation is 9.68%. The isolation performance and corresponding $\hat{s}_0(k)$ in one experiment are shown in Fig. 10. According to calculation, the isolation is 8.56%.

F. Experiment Conclusion

Referring to Section II.B and Tables II and III, the average isolations of PI, PI+NFFCS, PA-MRAC, and RLS-MRAC in experiments are 23.01%, 13.40%, 9.11%, and 9.68%, respectively. Compared to the PI+NFFCS, the isolation performances of the PA-MRAC and RLS-MRAC have increased by 32.01% and 27.76 %, respectively. It proves that the MRAC designed can further enhance the high-precision ISP's isolation performance.

Moreover, for the PA-MRAC, the maximum of $\hat{s}_0(k)$ in Fig. 9(b) is 0.048, the minimum is −0.099, and the range is 0.147. For the RLS-MRAC, those in Fig. 10(b) are 0.0030, −0.0061, and 0.0091, respectively, which means that the adjustment range of the PA-MRAC is larger. By normalizing $\hat{s}_0(k)$ of the two MRACs with the same mean of 1, the standard deviations of the PA-MRAC and the RLS-MRAC are 19.33 and 0.92,

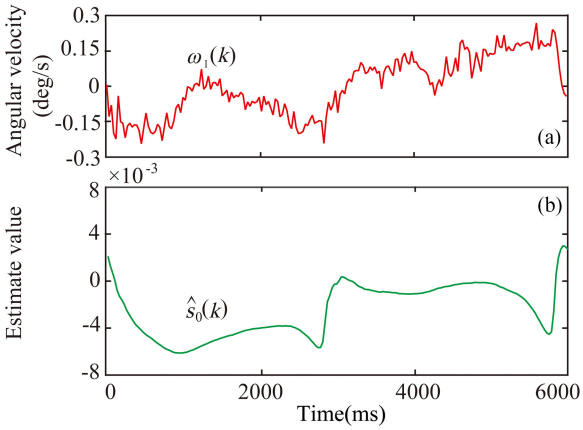

Fig. 10. Results of the turbulence isolation system with RLS-MRAC. (a) $\omega_1(k)$ curve. (b) $\hat{s}_0(k)$ curve.

respectively. It shows that variability of $\hat{s}_0(k)$ in PA-MRAC is stronger, and it has better ability to track the time-varying parameters. Hence, the PA-MRAC has better effects than the RLS-MRAC.

V. Conclusion

Based on the previous work on nonlinear friction modeling and compensation, this paper proposed a type of discrete-time direct MRAC to solve the problem of time-varying parameters. It has employed enhanced PA and the RLS with fading memory to respectively design the adaptive law. With the aid of the well-designed turbulence observer, the MRACs have been applied into the carrier turbulence isolation system, and the experiment results show they have further improved isolation performance. Due to the original controller's upgraded strategy, the proposed MRAC based on NFFCS has strong reliability and a high practical value.

Acknowledgment

K. Deng thanks all the researchers at the Key Laboratory of Aviation Optical Imaging and Measurement, Changchun, China, for their help during the experiments.

References

[1] J. M. Hilkert, "Inertially stabilized platform technology: Concepts and principles," *IEEE Control Syst.*, vol. 28, no. 1, pp. 26–46, Feb. 2008.
[2] Z. Hurak and M. Rezac, "Image-based pointing and tracking for inertially stabilized airborne camera platform," *IEEE Trans. Control Syst. Technol.*, vol. 20, no. 5, pp. 1146–1159, Sep. 2012.
[3] M. K. Masten, "Inertially stabilized platforms for optical imaging systems," *IEEE Control Syst.*, vol. 28, no. 1, pp. 47–64, Feb. 2008.
[4] J. Debruin, "Control systems for mobile Satcom antennas," *IEEE Control Syst.*, vol. 28, no. 1, pp. 86–101, Feb. 2008.
[5] M. W. Sun, Z. H. Wang, Y. K. Wang, and Z. Q. Chen, "On low-velocity compensation of brushless DC servo in the absence of friction model," *IEEE Trans. Ind. Electron.*, vol. 60, no. 9, pp. 3897–3905, Sep. 2013.
[6] J. Amin, B. Friedland, and A. Harnoy, "Implementation of a friction estimation and compensation technique," *IEEE Control Syst.*, vol. 17, no. 4, pp. 71–76, Aug. 1997.
[7] Z. Jamaludin, H. V. Brussel, and J. Swevers, "Friction compensation of an XY feed table using friction-model-based feedforward and an inverse-model-based disturbance observer," *IEEE Trans. Ind. Electron.*, vol. 56, no. 10, pp. 3848–3853, Oct. 2009.
[8] B. Armstrong-Helouvry, P. E. Dupont, and C. C. De Wit, "A survey of models, analysis tools and compensation methods for the control of machines with friction," *Autom.*, vol. 30, no. 7, pp. 1083–1138, Jul. 1997.
[9] J. Y. Yao, W. X. Deng, and Z. X. Jiao, "Adaptive control of hydraulic actuators with LuGre model-based friction compensation," *IEEE Ind. Electron. Soc.*, vol. 62, no. 10, pp. 6469–6477, Oct. 2015.
[10] W. S. Huang, C. W. Liu, P. L. Hsu, and S. S. Yeh, "Precision control and compensation of servomotors and machine tools via the disturbance observer," *IEEE Trans. Ind. Electron.*, vol. 57, no. 1, pp. 420–429, Jan. 2010.
[11] J. Q. Han, "From PID to active disturbance rejection control," *IEEE Trans. Ind. Electron.*, vol. 56, no. 3, pp. 900–906, Mar. 2009.
[12] X. J. Xie and J. L. Li, "A systematic analysis approach to discrete-time indirect model reference adaptive control," *Acta Autom. Sin.*, vol. 33, no. 11, pp. 1170–1175, Nov. 2007.
[13] C. Cao and N. Hovakimyan, "Stability margins of L_1 adaptive control architecture," *IEEE Trans. Autom. Control*, vol. 55, no. 2, pp. 480–487, Feb. 2010.
[14] P. A. Ioannou and A. M. Annaswamy, "L_1-adaptive control: Stability, robustness, and interpretations," *IEEE Trans. Autom. Control*, vol. 59, no. 11, pp. 3075–3080, Nov. 2014.
[15] R. Dey, S. K. Jain, and P. K. Padhy, "Robust closed loop reference MRAC with PI compensator," *IET Control Theory Appl.*, vol. 10, no. 18, pp. 2378–2386, Dec. 2016.
[16] U. Montanaro, A. di Gaeta, and V. Giglio, "Robust discrete-time MRAC with minimal controller synthesis of an electronic throttle body," *IEEE/ASME Trans. Mechatron.*, vol. 19, no. 2, pp. 524–537, Apr. 2014.
[17] L. E. G. Castanon, A. V. Martinez, and R. C. Reynoso, "MRAC-based fault tolerant control of a SISO real process application," *IEEE Latin Amer. Trans.*, vol. 13, no. 8, pp. 2545–2550, Aug. 2015.
[18] Y. B. Zbede, S. M. Gadoue, and D. J. Atkinson, "Model predictive MRAS estimator for sensorless induction motor drives," *IEEE Trans. Ind. Electron.*, vol. 63, no. 6, pp. 3511–3521, Oct. 2016.
[19] W. C. Sun, Y. F. Zhang, Y. P. Huang, H. J. Gao, and O. Kaynak, "Transient-performance-guaranteed robust adaptive control and its application to precision motion control systems," *IEEE Trans. Ind. Electron.*, vol. 63, no. 10, pp. 6510–6518, Oct. 2016.
[20] Z. Wang, R. Q. Lu, F. R. Gao, and D. R. Liu, "An indirect data-driven method for trajectory tracking control of a class of nonlinear discrete-time systems," *IEEE Trans. Ind. Electron.*, vol. 64, no. 5, pp. 4121–4129, Oct. 2017.
[21] M. B. Rădac, R. E. Precup, E. M. Petriu, and S. Preitl, "Iterative data-driven tuning of controllers for nonlinear systems with constraints," *IEEE Trans. Ind. Electron.*, vol. 61, no. 11, pp. 6360–6368, Nov. 2014.
[22] Y. Yang, S. N. Balakrishnan, L. Tang, and R. G. Landers, "Electrohydraulic control using neural MRAC based on a modified state observer," *IEEE/ASME Trans. Mechatronics*, vol. 18, no. 3, pp. 867–877, Jun. 2013.
[23] S. Cong, K. Deng, D. J. Kong, and H. H. Sheng, "Isolation control for inertially stabilized platform based on nonlinear friction compensation," *Nonlinear Dyn.*, vol. 84, no. 3, pp. 1123–1133, May 2016.
[24] D. Putra, H. Nijmeijer, and N. van de Wouw, "Analysis of undercompensation and overcompensation of friction in 1DOF mechanical systems," *Automatica*, vol. 43, no. 8, pp. 1387–1394, Aug. 2007.
[25] S. Akhtar and D. S. Bernstein, "Lyapunov-stable discrete-time model reference adaptive control," *Int. J. Adapt. Control Signal Process.*, vol. 19, no. 10, pp. 745–767, Dec. 2005.

Ke Deng was born in Meishan, China, in 1985. He received the B.E degree in automation and the Ph.D. degree in systems engineering from the University of Science and Technology of China, Hefei, China, in 2009 and 2016, respectively.

He is currently an Engineer with the State Key Laboratory of Air Traffic Management System and Technology, Nanjing, China. His research interests include nonlinear modeling analysis, advanced control strategies, and systems engineering.

Shuang Cong (M'07–SM'12) received the B.E. degree in automation from Beijing University of Aeronautics and Astronautics, Beijing, China, in 1982, and the Ph.D. degree in system engineering from the University of Rome La Sapienza, Rome, Italy, in 1995.

She is currently a Professor with the Department of Automation, University of Science and Technology of China, Hefei, China. Her research interests include advanced control strategies for motion control, fuzzy logic control, neural networks design and applications, robotic coordination control, and quantum systems control.

Dejie Kong received the Master's degree in power electronics and electric drives from Shandong University, Jinan, China, and the D.E. degree in optical engineering from the University of Chinese Academy of Sciences, Beijing, China, in 2002 and 2014, respectively.

From 2005 to 2009, he was an Assistant Engineer with the Changchun Institute of Optics Fine Mechanics and Physics. From 2009 to 2014, he was an Assistant Professor with the Changchun Institute of Optics Fine Mechanics and Physics. Since 2017, he has been an Associate Professor with the Changchun University of Science and Technology , Changchun, China, where he is mainly engaged in inertial platform stabilization platform control, as well as motor control and drive research.

Honghai Shen received the Master's degree in mechanical and electrical engineering from the Chinese Academy of Sciences, Beijing, China, in 2001.

In 2001, he joined the Changchun Institute of Optics, Mechanics and Physics, Chinese Academy of Science, Changchun, Jilin, China, where he is currently the Director of the Key Laboratory of Aviation Optical Imaging and Measurement, Changchun, China. His research interests include control and optimization algorithms applied to motor drives systems.